Correspondence Between "Stable" Flame Macrostructure and Thermo-acoustic Instability in Premixed Swirl-Stabilized Turbulent Combustion

Soufien Taamallah[1]
Reacting Gas Dynamics Laboratory,
Mechanical Engineering Department,
MIT,
Cambridge, MA 02139

Zachary A. LaBry
Reacting Gas Dynamics Laboratory,
Mechanical Engineering Department,
MIT,
Cambridge, MA 02139

Santosh J. Shanbhogue
Reacting Gas Dynamics Laboratory,
Mechanical Engineering Department,
MIT,
Cambridge, MA 02139

Mohamed A. M. Habib
Mechanical Engineering Department,
KFUPM,
Dhahran 34464, Saudi Arabia

Ahmed F. Ghoniem
Reacting Gas Dynamics Laboratory,
Mechanical Engineering Department,
MIT,
Cambridge, MA 02139

In this paper, we conduct an experimental investigation to study the link between the flame macroscale structure—or flame brush spatial distribution—and thermo-acoustic instabilities, in a premixed swirl-stabilized dump combustor. We operate the combustor with premixed methane–air in the range of equivalence ratio (ϕ) from the lean blowout limit to $\phi = 0.75$. First, we observe the different dynamic modes in this lean range as ϕ is raised. We also document the effect of ϕ on the flame macrostructure. Next, we examine the correspondence between dynamic mode transitions and changes in flame macrostructure. To do so, we modify the combustor length—by downstream truncation—without changing the underlying flow upstream. Thus, the resonant frequencies of the geometry are altered allowing for decoupling the heat release rate fluctuations and the acoustic feedback. Mean flame configurations in the modified combustor and for the same range of equivalence ratio are examined, following the same experimental protocol. It is found that not only the same sequence of flame macrostructures is observed in both combustors but also that the transitions occur at a similar set of equivalence ratio. In particular, the appearance of the flame in the outside recirculation zone (ORZ) in the long combustor—which occurs simultaneously with the onset of instability at the fundamental frequency—happens at similar ϕ when compared to the short combustor, but without being in latter case accompanied by a transition to thermo-acoustic instability. Then, we interrogate the flow field by analyzing the streamlines, mean, and rms velocities for the nonreacting flow and the different flame types. Finally, we focus on the transition of the flame to the ORZ in the acoustically decoupled case. Our analysis of this transition shows that it occurs gradually with an intermittent appearance of a flame in the ORZ and an increasing probability with ϕ. The spectral analysis of this phenomenon—we refer to as "ORZ flame flickering"—shows the presence of unsteady events occurring at two distinct low frequency ranges. A broad band at very low frequency in the range ~(1 Hz–10 Hz) associated with the expansion and contraction of the inner recirculation zone (IRZ) and a narrow band centered around 28 Hz which is the frequency of rotation of the flame as it is advected by the ORZ flow. [DOI: 10.1115/1.4029173]

1 Introduction

Premixed combustion is considered as one of the most effective methods to reach low NO_x emissions and comply with increasingly stringent regulation. Combined with swirling flow geometries, very lean operation is possible, making single digit NO_x emissions a reality. However, premixed combustion technology still faces some difficulties; one of the most prominent challenges is the increased susceptibility to thermo-acoustic instabilities that can lead to safety issues and potentially have dramatic and irreversible consequences on costly gas turbine hardware. Heat release from the reacting flow can experience fluctuations often due to equivalence ratio oscillations or unsteadiness in the flow field itself, like vortex shedding and other coherent flow structures. Heat release oscillations may couple with the acoustic pressure fluctuations to form a positive feedback loop that can lead, under some conditions, to resonance. Most operating conditions have been shown to influence the thermo-acoustic stability of the combustor. Equivalence ratio as well as fuel composition, mixture preheat temperature, and other flow properties like swirl and Reynolds numbers' effect on dynamic instabilities have been investigated [1–8]. Because of its critical importance, thermo-acoustic instabilities arising in premixed combustion have been extensively studied for decades and are still an active area of research. However, our knowledge in this field is still incomplete and more research effort is needed. Candel [9] provides a comprehensive review of the challenges pertaining to combustion instabilities and the advances made in modeling, predicting, and controlling it. A more recent review by Huang and Yang [10] focused on dynamic instabilities in swirl-stabilized combustors, looking at both experimental and numerical progress made in this field; different driving mechanisms for instabilities were surveyed as well as the existing methods for mitigating this unwanted phenomenon both in a passive and active fashion.

Modern gas turbine combustors rely on turbulent swirl-stabilized combustion as an effective way to anchor the flame and lower the blowout limit at lean operations. These complex swirling flows give rise to multiple recirculation zones and shear layers creating many possibilities of flame local stabilization. This makes swirling reacting flows exhibit several possible mean flame configurations. These flame brush distributions,

[1]Corresponding author.

Contributed by the Combustion and Fuels Committee of ASME for publication in the Journal of Engineering for Gas Turbines and Power. Manuscript received September 22, 2014; final manuscript received October 31, 2014; published online December 23, 2014. Editor: David Wisler.

which we refer to as macroscale structures or simply macrostructures, have also been previously reported as a function of different operating conditions. Schefer et al. reported the dependency of flame macrostructures on fuel composition through hydrogen addition to a premixed air–methane mixture [11]. Chterev et al. explored the effect of equivalence ratio and preheat temperature as well as geometrical features like the swirl number and the centerbody design on the different mean flame configurations [12,13]. The dependency of flame macrostructures on the Reynolds number has been also investigated. The common flame macrostructures often observed in swirl-stabilized combustors are as follows: columnar flames; bubble-columnar flames; conical flames with no flame stabilized in the ORZ; and conical flames with reaction taking place in the ORZ and/or along the OSL. Depending on the geometry and the burner centerbody, some of these flames have also been observed both attached or lifted from the centerbody.

It is essential to understand the controlling parameter for different flame macrostructures. The conditions under which transitions between flame types and the mechanisms underlying it are of great interest. One of the main reasons is the potential shift in dynamic stability characteristics of certain combustors when changes in flame macrostructure occur. Few researchers highlighted this relationship. By changing the inlet temperature in their large eddy simulation of swirl-stabilized combustion, Huang et al. noted that there is a temperature threshold where the flame propagated into the ORZ. This change in flame macrostructure was accompanied by a bifurcation to thermo-acoustic instability. The author argued that the presence of the flame in the ORZ makes the combustor more prone to instability, since a large amount of heat is released within a confined area close to an acoustic antinode [10]. Such results favor a hypothesis of causality from a transition to ORZ flame to an onset of thermo-acoustic instabilities. In a study spanning a wider range of operating conditions, Fritsche et al. investigated both optical and acoustic characteristics of flames at different conditions: one of the goal was to explore the connections existing between flame types and noise levels. They showed that flame shapes closer to the lean blowout, i.e., the columnar flames and single conical flames are always dynamically stable, and that the flames with reactions taking place in the ORZ can be stable or unstable depending on the choice of equivalence ratio and inlet temperature. The transition to thermo-acoustic instability as the equivalence ratio is increased, for a fixed inlet temperature, occurred along with the first appearance of a continuous flame front in the ORZ. Figura et al. chose to investigate fuel composition effect on dynamic instabilities in a lean premixed combustor through changing the combustion length and hydrogen fraction in a natural gas-hydrogen mixture. They reached the conclusion that operating conditions with "the same stable flame location have very similar stability characteristic."

Thus, the relationship between flame macrostructures and dynamic stability has been observed but few systematic investigations of this relationship, spanning all possible macrostructures were undertaken. In addition, it is still unclear from the previous studies whether acoustic fluctuations are responsible for the flame macrostructures to change (in particular the propagation into the ORZ for double conical flames) or the presence of the flame in the ORZ leads to a sharp increase in sound levels. More evidence is needed to know if flame macrostructure transition is acoustically dominated or turbulent combustion dominated phenomenon. In this paper, we explore the relationship between the flame configuration in a swirl-stabilized combustor at different equivalence ratios and its stability map, in more detail, by controlling the effect of acoustics. We focus on the equivalence ratio over the lean operating range $\phi \in [\phi_{LBO} - 0.75]$, keeping everything else fixed (fuel, swirl number, Reynolds number, inlet temperature, and pressure). We first describe the experimental setup as well as the diagnostics techniques used in this study. Then, we analyze the dynamic stability map of the combustor and different mean configurations exhibited by the flame as the equivalence ratio is raised. A modification of the combustor without changing the underlying flow allows the decoupling of the combustion and the acoustics over a range of interest. A comparison of the mean flame configurations obtained for both combustor lengths is done. Finally, we focus on the transition to an ORZ flame and extract some of the dynamics associated with it.

2 Experimental Setup and Diagnostics

2.1 Experimental Apparatus. Experiments are conducted in a swirl-stabilized dump combustor representative of can combustors found in modern gas turbines. Figure 1 shows the details of the experimental setup used in this study. Fuel and air are premixed upstream of a choke plate. The role of the choke plate used here is twofold. First, by choking the flow, a sonic Mach number is imposed preventing pressure waves from traveling upstream. The fuel and air nozzles would not be disturbed by acoustic waves avoiding equivalence ratio fluctuations. Thus, we allow mainly vortex-driven combustion dynamics in this investigation. Second, the use of an orifice plate ensures close to perfect premixedness of the fuel and air before reaching the combustion chamber.

After the choke plate the mixture flows through a cylindrical pipe with inner diameter of $D_{inlet} = 38$ mm and length $L_{inlet} = 14.2 \times D_{inlet}$, i.e., sufficient length to reach quasi-full development of the flow. An axial eight-vane swirler with a streamlined centerbody and 45 deg vane angle shown in Fig. 2 placed at a distance $L_{swirler} = 11.6 \times D_{inlet}$ downstream of the choke plate and $2.6 \times D_{inlet}$ upstream of the expansion plane is used to provide the flow with an azimuthal component before entering the combustion chamber. Swirling flows are widely used in modern combustors. The vortex breakdown exhibited by swirling flows at some swirl and Reynolds numbers conditions contribute to stronger flame anchoring. A comprehensive review of swirling flows was written by Lucca-Negro and O'Doherty [14].

After the swirler, the flow passes through a sudden expansion from the upstream diameter to a downstream diameter $D_{outlet} = 2 \times D_{inlet}$. Sudden expansions are also commonly used in combustor as they force flow separation and create shear layers and recirculation zones. Finally, the exhaust plane is situated at $L_{exhaust} = 115.8 \times D_{inlet}$ downstream of the choke plate. The combustor discharges into a plenum at near atmospheric pressure. The experimental setup is similar to the ones previously investigated by our research group [15–18]. The swirl number is fixed and estimated at $S \sim 0.7$ based on the swirler's vanes angle, the Reynolds number based on the inlet diameter is $Re_{D_{in}} = 20,000$, and the pressure is atmospheric. At these conditions, a vortex breakdown occurs downstream of the swirler due to an adverse pressure gradient both in the nonreacting and reacting flows, creating a central recirculation zone. The presence of a sudden expansion exacerbates the adverse pressure gradient, stabilizes the axial location of the IRZ, and also creates an additional toroidal recirculation zone outside of the main jet, leaving the inlet pipe called outer recirculation zone (ORZ). An inner and outer shear layers (ISL and OSL) separate the three zones: the IRZ, the annular swirling jet, and the ORZ, as shown schematically in Fig. 3.

2.2 Diagnostics Tools. Different diagnostics techniques are used in this paper. Pressure measurements are performed in the combustor at $L_{P1} \approx 3 \times D_{inlet}$ downstream of the choke plate using a Kulite MIC-093 microphone. High speed chemiluminescence flame imaging is performed using a NAC GX-1 high-speed CMOS camera mounted on the side of the combustor. The high speed camera is equipped with an infrared (IR) blocking CG-BG-39 Schott filter. A 50 mm lens with an aperture value of $f/1.8$ is used at frame rates varying from 100 to 200 frames per second and an exposure time of 1/250 s. Larger exposure time flame images are taken using a digital single-lens reflex (DSLR) camera, from which the flame brush extent—we refer to as the flame

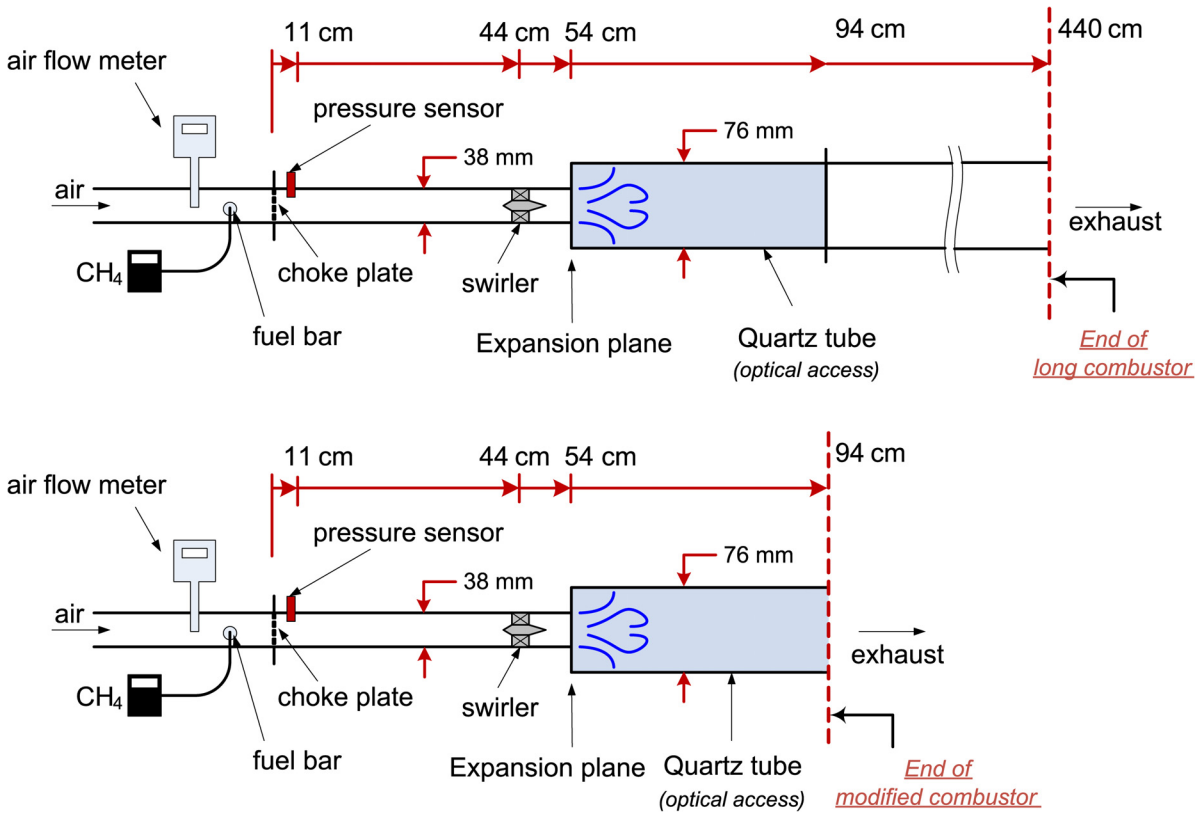

Fig. 1 Long and short geometries for acoustic-heat release decoupling

macrostructure—is inferred. The DSLR camera is equipped internally with a built-in IR cut filter at the sensor level as well as a glass lens eliminating part of the IR radiation and no external filter were used. The long exposure chemiluminescence images using the DSLR camera are taken with exposure time of 1/4 s, an aperture value of *f*/2.8, and ISO (sensor sensitivity) of 3200. Optical access is made possible via a fused silica tube of length $L_{\text{quartz tube}} = 10.5 \times D_{\text{inlet}}$ and thickness $\delta_{\text{quartz}} = 2.5$ mm, shown in Fig. 1. The obtained line-of-sight mean flame images are deconvolved using an inverse Abel transform [19]. This operation leads to a single cross-sectional distribution of the flame and gives the spatial range of the flame brush.

The velocity field is interrogated using a high-speed particle image velocimetry (PIV) system. Al_2O_3 seeding particles (of diameter between 0.9 and 2.2 μm) are introduced into the mixture upstream of the swirler. A light sheet less than 1 mm thick is produced along the combustor's axis using a 50 W Nd:YLF laser. Two high-speed NAC GX-1 CMOS cameras are mounted aside and above the combustor, recording images at 1 kHz. At each condition, three ensembles of data are recorded with a duration of 0.5 s each to reach statistically meaningful mean and RMS (root mean square) values. A statistical uncertainty analysis on the PIV data was performed by computing the standard error of the mean. For axial velocities, we obtained a precision uncertainty of 12.32 ± 0.11 m · s^{-1} for the maximum absolute value and 0 ± 0.07 m · s^{-1} for the minimum absolute value, with 95% confidence. For radial velocities, we have a precision uncertainty of 6.9 ± 0.1 m · s^{-1} for the maximum absolute value and 0 ± 0.034 m · s^{-1} for the minimum absolute value, with 95% confidence.

Methane is supplied by a Sierra C100M Smart-Trak digital mass flow controller with a flow rate uncertainty of $\pm 1\%$ of maximum capacity. A Sierra Instruments 780 S Flat-Trak flow meter is used to measure the air flow rate with the same uncertainty. Subsequent measurement error on the equivalence ratio is $\delta\phi_{\text{error}} \approx 0.002$.

3 Results and Discussion

3.1 Dynamic Instabilities and Flame Macrostructures. The stability map of pure methane combustion in the atmospheric pressure swirl-stabilized combustor is determined first: we

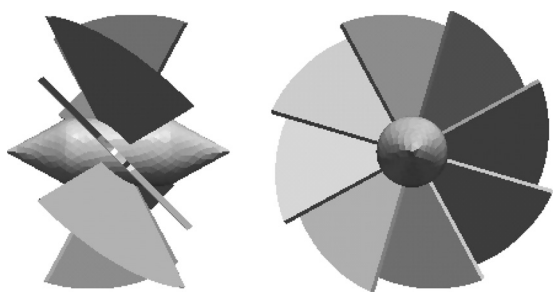

Fig. 2 Axial eight-vane swirler with 45 deg vane angle and a streamlined centerbody with a diameter of 9 mm and a 60 deg cone angle

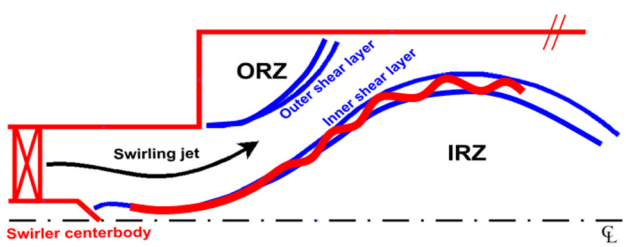

Fig. 3 Schematic flow field in the swirl-stabilized combustor: ORZ, annular incoming swirling jet, and IRZ regions delimited by the outer and inner shear layers, in the mean flow sense

increase the equivalence ratio from near the lean blowoff limit (LBO limit at 0.47 for pure methane in these conditions) up to 0.75 (below flashback). Each increment of $\delta\phi = 0.01$ is maintained for a $\delta t = 10$ s interval. This value is chosen to allow enough time for the equivalence ratio to stabilize around a set point and to provide a large enough Fourier number to ensure close to thermal steady state at the boundary ($F_o = \alpha_{\text{quartz}}\delta t/\delta^2_{\text{quartz}} \approx 2$).

At low equivalence ratios—close to LBO limit—combustion is stable and the recorded pressure fluctuation is relatively low (oscillating between ± 50 Pa). As the equivalence ratio is raised the first unstable mode appears, before the combustor becomes quiet again. A further increase in the equivalence ratio leads to a second unstable mode. Figure 4(*b*) shows the evolution of the pressure fluctuations upstream of the swirler as the equivalence ratio is raised. The solid line on the left corresponds to the LBO limit. Figure 4(*c*) shows the associated spectrogram on which we can differentiate five regions. The first region extends from LBO until $\phi \sim 0.55 - 0.56$. In this range, combustion is stable with a broadband turbulent combustion noise. No coupling with the acoustic field is taking place. Starting at $\phi = 0.56$ pressure fluctuations with a 38–40 Hz dominant harmonic but still with low amplitude appear. A weak coupling between combustion and the acoustic field takes place. As the equivalence ratio is raised further, a transition to the first unstable mode with a 40–42 Hz dominant frequency and large sound pressure level (around 145 dB) takes place. The onset of this instability occurs around $\phi = 0.61$. This region extends for a $\Delta\phi \approx 0.03$ beyond which a quasi-stable combustion appears again, similar to the quasi-stable region

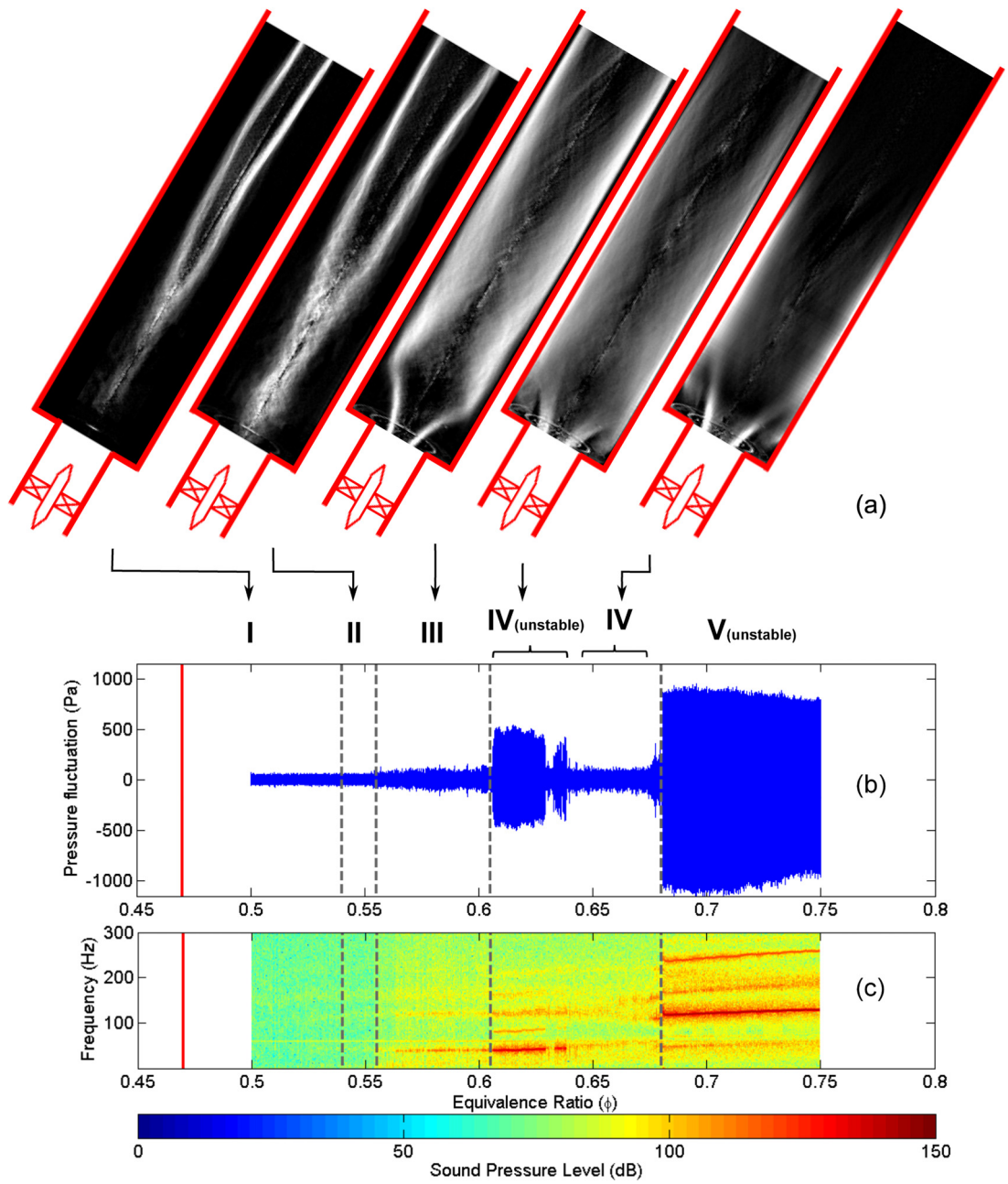

Fig. 4 Correspondence between the observed mean swirling flame configurations (roman numerals) and dynamic mode transitions in the long combustor for methane. The equivalence ratio was changed from $\phi = 0.5$ to $\phi = 0.75$ in upward increments of $\Delta\phi = 0.01$. (*a*) Mean swirling flame configurations. (*b*) Pressure fluctuations signal. (*c*) Associated spectrogram. Solid line at $\phi = 0.47$ represents the LBO limit. Dotted lines represent the transitions between mean flame configurations.

observed for $\phi \in [0.56 - 0.61]$. When the equivalence ratio reaches $\phi = 0.68$, an abrupt increase of the sound pressure level occurs and a dominant oscillatory component appears at 117 Hz with a large sound pressure level around 150 dB. Table 1 summarizes the characteristic of the different regions observed. Similar dynamic modes have been previously reported by Speth et al. [20] using different syngas mixtures in a similar geometry.

The spatial distribution of the flame brush changes as the equivalence ratio is raised. The mechanisms underlying these changes are still not fully understood. In the current paper we do not attempt to explain the reasons behind the transition between flame configurations but we focus instead on establishing the relationship between the mean flame configurations and the dynamic modes observed.

Figure 4(*a*) shows the sequence of mean flame configurations observed. For a fixed swirl and Reynolds numbers, the flame configuration changes, along with the sound pressure level observed earlier. The transitions in mean flame configurations are marked by the vertical dotted lines in Figs. 4(*b*) and 4(*c*). At low equivalence ratio, close to the LBO limit, the flame appears in a columnar shape in the shear layer delimiting the vortex core downstream of the vortex breakdown (flame I). As the equivalence ratio increases, the columnar distribution gets wider and a transition occurs at a certain value of the equivalence ratio ($\phi \sim 0.54$). The flame propagates inside and around the vortex breakdown bubble as well as along the shear layer defining the portion of the vortex core upstream of the breakdown (flame II). The flame is observed to extend inside the inlet tube reaching the swirling centerbody. This flame exists in a relatively narrow range of equivalence ratio. The downstream portion of the flame is still columnar, similar to flame I, but with a larger diameter. Flame III appears suddenly (i.e., change occurs within a $\Delta\phi = 0.01$). In this configuration, the flame brush appears close to the combustion chamber wall boundary layer. The major difference with the previous configuration is that combustion is not taking place inside the IRZ. A comparison between the mean flame chemiluminescence and the pressure measurement (see Fig. 4) shows that this transition (II to III) is accompanied by the transition from stable to quasi-stable dynamic mode (region 2 to 3 described above), i.e., to the weakly oscillating 40 Hz mode. Increasing the equivalence ratio leads to a more and more compact flame but still with the same overall mean configuration, i.e., still flame III. At an equivalence ratio between 0.6 and 0.61, the onset of the first unstable mode is accompanied by a flame configuration change. The flame transitions from configuration III to a configuration IV where on average the flame appears along the inner shear layer but also extends to the ORZ and OSL. When combustion becomes quasi-stable again (region 4 in Table 1), the flame on average still appears in the inner shear layer, extending close to the wall, and remains also in the ORZ. At higher equivalence ratio, the sudden sound pressure level jump happens simultaneously with another transition in the mean flame structure. This corresponds to another configuration (flame V). The latter configuration is highly unsteady, oscillating at higher frequency, starting around 117 Hz. Flame V is not shown here and a phase-average analysis is more appropriate for this highly unsteady flame but this transition is out of the scope of the current study.

Superposing the sound pressure level and the mean chemiluminescence signal from the flame in Fig. 4 shows a clear correspondence between the mean flame distribution—as reflected by the flame macrostructures I to V—and the dynamic behavior of the combustor. Some transition in flame macrostrucutres did not change the acoustic energy of the combustor (flame I to II) whereas other transitions (II to III and III to IV) were accompanied by a measurable change. It is important to see here that the first appearance of a continuous flame front in the ORZ (flame IV) as the equivalence ratio is raised matches with the onset of the first unstable mode. Moreover, flame IV can be unstable and quasi-stable. This is similar to the "noise island" previously reported by Fritsche et al. [8]. In the next section (Sec. 3.2), we analyze further the changes in dynamic mode of the combustor and explore any potential causality between flame shape transition and onset of instabilities.

3.2 Acoustically Decoupled Combustion Analysis

3.2.1 Acoustic Decoupling. In order to examine in more detail the onsets of unstable modes, we artificially decouple heat release fluctuations from the acoustic field. The method used for decoupling is the modification of the combustor's geometry downstream to alter the resonant frequencies without changing the underlying flow. By doing so, we break the feedback loop between unsteady heat release and acoustic pressure fluctuations. The eigenfrequencies of a combustor depend to a large extent on the geometry and the temperature distribution as these are the main sources of acoustic impedance change. Here, the combustor is shortened to achieve the decoupling of heat release and pressure in a range of equivalence ratio of interest. Figure 1 shows the geometry after changing the combustor's length. These two lengths lead to combustors with different sets of resonant frequencies.

The length of the combustor in both cases is larger than the largest diameter allowing for a one-dimensional modeling of the geometry. By taking into account a simple impedance change due to the presence of the flame, the resonant frequencies are estimated for both configurations. This simplified quasi-one-dimensional model assumes the flame as compact and doesn't take into account the flame transfer function. The flame, in this model, is only responsible for a sudden change in the flow temperature.

Figure 5 shows the numerically predicted resonant frequencies of the initial length combustor as a function of the equivalence ratio (left) and these frequencies when the combustor is shortened by a factor of ~10 (right). At $\phi = 0.61$ (onset of instability in region 3 shown previously) the first eigen-mode is estimated around 49 Hz which is in fair agreement with the frequency observed experimentally (40 Hz—see spectrogram in Fig. 4). At $\phi = 0.68$ where region 5 instability starts, the second eigen-mode is estimated around 142 Hz to be compared to the frequency observed experimentally (117 Hz). After altering the length of the combustor, the two resonant modes mentioned above are shifted to higher frequencies and appear around 155 Hz and 440 Hz, respectively. The comparison of the predicted and experimental resonant frequencies shows a fair agreement for the long combustor. A non-negligible discrepancy appears for the case of the short combustor, as will be seen later. This shows the limit of a simple one-dimensional modeling for this case where the assumptions made, like a compact flame, a large aspect ratio of the combustor, become more debatable.

Table 1 Dynamic modes and characteristics for the long combustor

	Equivalence ratio	Dominant frequency	Dynamic mode	Mean flame configuration
Region 1	0.50–0.555	Broadband	Stable	I and II
Region 2	0.555–0.61	~38–40 Hz (low amplitude)	Quasi-stable	III
Region 3	0.61–0.64	~40–42 Hz	First unstable mode	IV
Region 4	0.64–0.67	~48–55 Hz (low amplitude)	Quasi-stable	IV
Region 5	0.67–0.75	~117–129 Hz	Second unstable mode	V

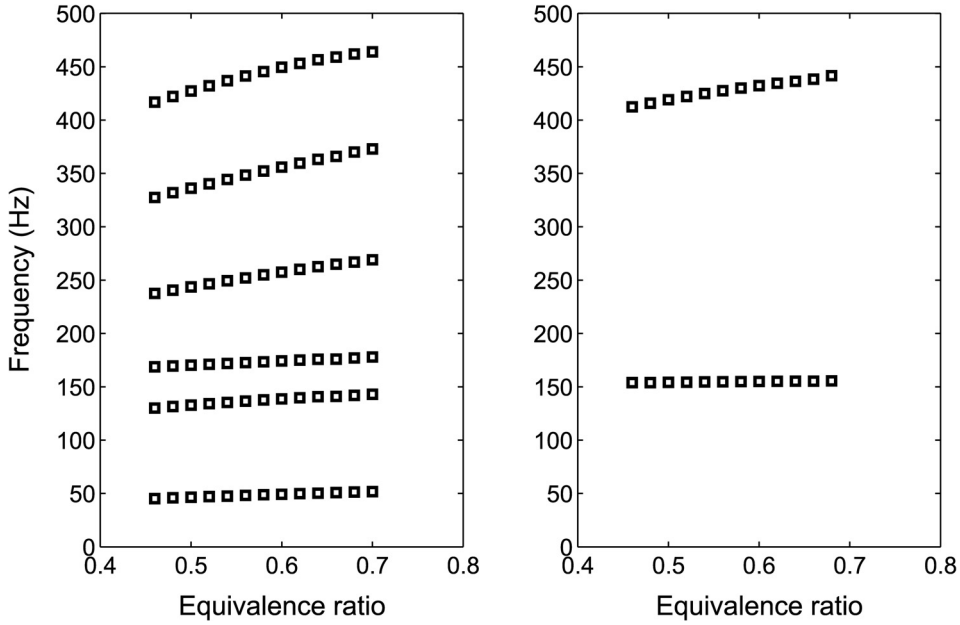

Fig. 5 Predicted longitudinal modes of the combustor (left: long, right: short) using one-dimensional acoustic calculation

Pressure fluctuations in the nonreacting flow and a near blowout (flame I) conditions are shown for comparison to further assess the above predictions. Figure 6 confirms the fair agreement found with predictions using the simplified acoustic network approach. We see that the natural frequency of the combustor is shifted to higher values, as expected with a shorter length. Additional peaks are observed in Fig. 6; these are potentially the results of nonlinear interaction between acoustic modes and a precessing vortex core (PVC) [21] observed in cold flow and in flame configuration I. The PVC frequency is observed in the range of 100–120 Hz, which is close to the second harmonic of the long combustor and the fundamental frequency of the short combustor. We also note the effect of the combustion and its heat release on the natural frequencies of the combustor.

3.2.2 Dynamic Stability and Flame Macrostructures in the Long Versus Short Combustor. We conduct the same series of experiments to determine the stability map of methane combustion

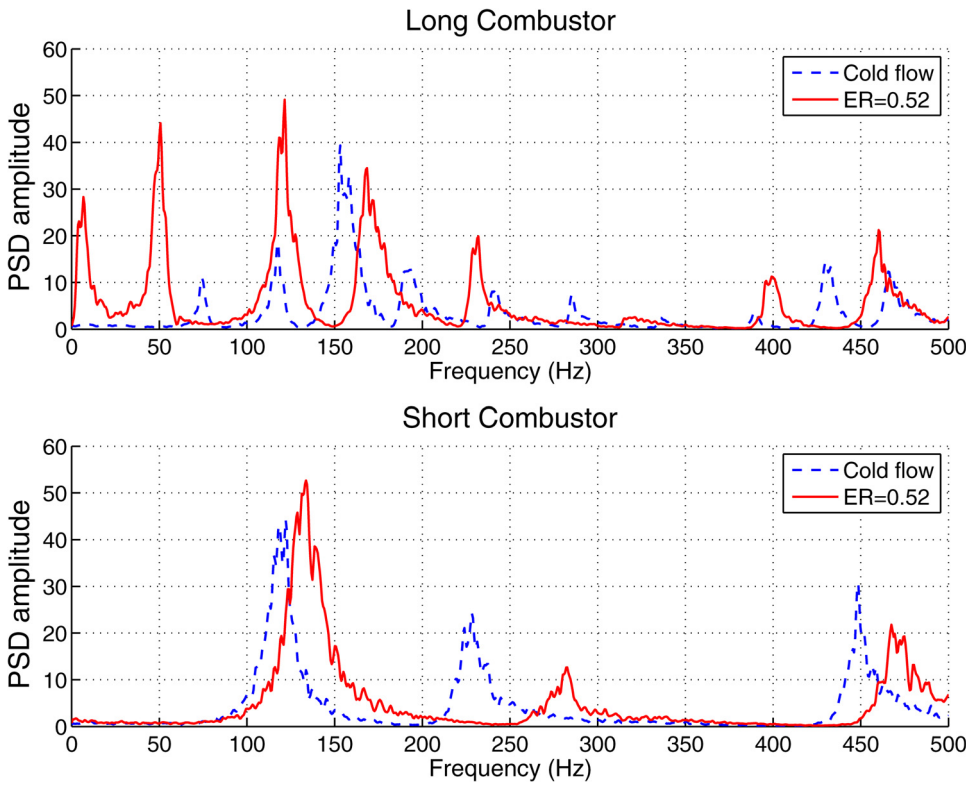

Fig. 6 Experimental measurements of the combustors' natural frequencies, to be compared with the predicted frequencies in Fig. 5 (top: long combustor, bottom: short combustor)

in the modified combustor. A special care was given to ensure the same experimental protocol for both combustors. We first see that the 40 Hz unstable mode is fully suppressed in the short combustor. We see also that combustion in the two previous quasi-stable regions is now fully stable. The short combustor still exhibits an unstable mode for equivalence ratio above $\phi \sim 0.7 - 0.71$ but with lower amplitude. The modification of the geometry succeeded in completely decoupling combustion from the acoustic field for equivalence ratio between the LBO up to $\phi \sim 0.7 - 0.71$.

When decoupling the acoustics from the heat release fluctuations, the swirling reacting flow in the short combustor still exhibits several flame macrostructures as we raise the equivalence ratio. As done previously, the mean flame distribution is inferred from long exposure flame imaging. Figure 7(*b*) shows the different mean flame configurations observed as the equivalence ratio is raised.

The five configurations observed earlier are still observed. However, while the transition III to IV was previously accompanied by the onset of an unstable mode at the fundamental frequency of the long combustor, the transition occurs while the combustor remains stable, in the shortened version. This transition occurs gradually starting from $\phi \sim 0.61$. The flame starts to appear intermittently in the outer recirculation zone. Figure 8 shows a sequence of high speed flame images taken at a frame rate of 200 fps with an exposure time of 1/200 s, illustrating this intermittency and in which we see a flame appearing in the ORZ, disappearing and re-appearing again. This phenomenon is referred to as ORZ flame flickering. ORZ flickering extends over a range $\Delta\phi \approx 0.03$ beyond which the flame becomes present in the ORZ with a probability close to 1 (as will be seen in Sec. 3.3) which corresponds to configuration IV.

Following the same approach as that used for the long combustor, we superpose the measured pressure signal—as the equivalence ratio is raised—and the different flame configurations observed. The result is shown in Fig. 9 where transition points are carefully noted and ensemble-averaged over three experiments, performed following the same experimental protocol. We see that the observed sequence of mean flame configurations is not only the same in the long and short combustors, but the transitions (for configurations I, II, III, and IV) occur at similar equivalence ratios as well. However, the transition from configuration IV to V occurs at a higher equivalence ratio compared to the long combustor case. Moreover, the ORZ flame flickering window between $\phi \sim 0.61$ and $\phi \sim 0.64/0.65$, overlaps with the range of equivalence ratio at which the long combustor exhibits its first unstable

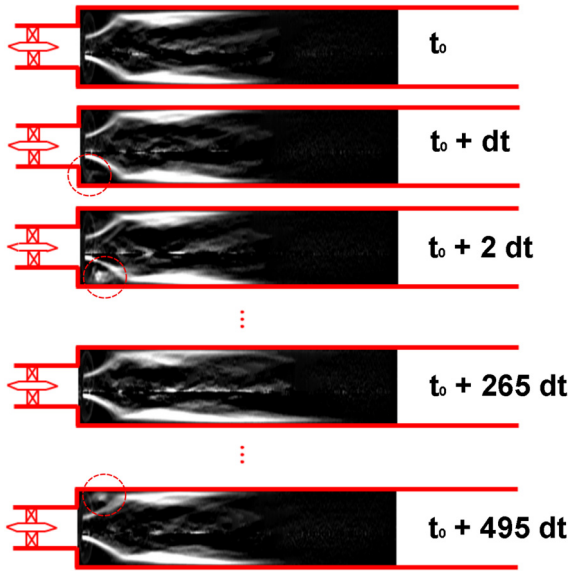

Fig. 8 Sequence of high speed flame chemiluminescence images (200 fps, exposure time of 1/200 s) showing the intermittent appearance of flame in the ORZ in the short combustor. Here, d*t* is the time step between two images, $\phi = 0.62$. Dotted circle shows flame in the ORZ.

mode. Table 2 summarizes the combustion characteristics for both combustor lengths.

3.2.3 Flow Field of Stable Flame Macrostructures. We now interrogate the flow field, in the decoupled short combustor, for each of the flame macrostructures (I to IV) using PIV. Under these conditions, these configurations are all dynamically stable. The velocity field undergoes dramatic changes as we transition from a configuration to another, highlighting the strong coupling between the turbulent flow and the heat release. Figures 10 and 11 show the time-averaged axial–radial velocity streamlines colored by the velocity magnitude and the total rms velocity, respectively. In addition, the zero axial velocity contour is shown, as an approximate location of the mean shear layer. Only axial and radial velocities were measured so the mean velocity magnitude is estimated as

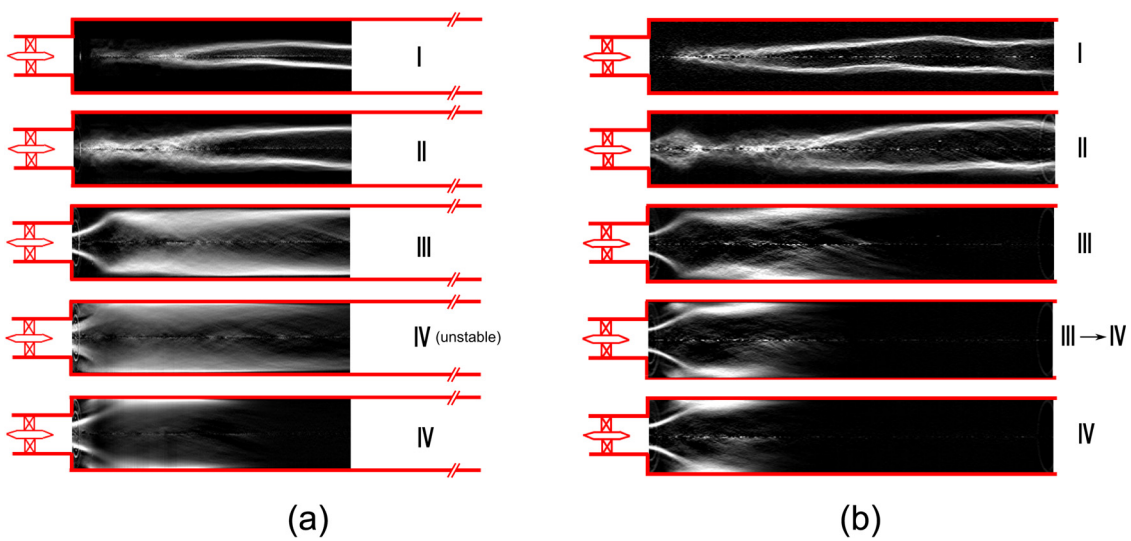

Fig. 7 Observed swirling flame configurations as the equivalence ratio is raised from the LBO limit in the long (*a*) and short combustors (*b*). From top to bottom: ϕ: 0.51, 0.54, 0.57, 0.62, and 0.66.

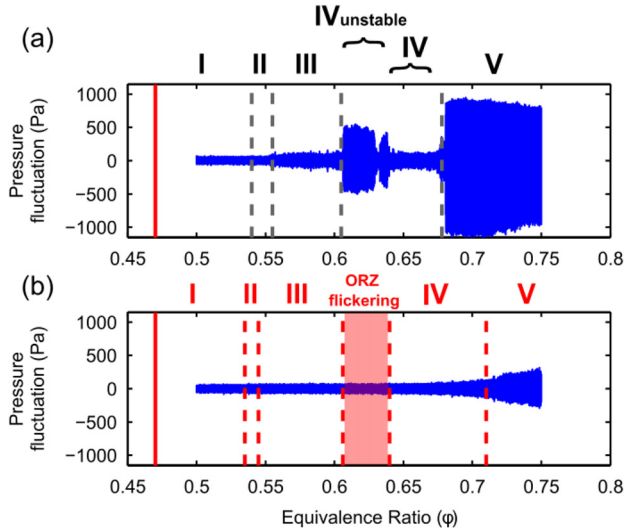

Fig. 9 Correspondence between the observed mean swirling flame configurations and dynamic mode transitions in long (*a*) and short (*b*) combustors. Vertical solid lines represent the LBO limit and dotted lines represent the transitions between flame configurations.

$$V_{\mathrm{mag,mean}} = \sqrt{[U^2_{x,\mathrm{mean}} + U^2_{r,\mathrm{mean}} + U^2_{\theta,\mathrm{mean}}]} \quad (1)$$

$$\approx \sqrt{[U^2_{x,\mathrm{mean}} + U^2_{r,\mathrm{mean}} + (SU_{x,\mathrm{mean}})^2]} \quad (2)$$

with S being the swirl number and $SU_{x,\mathrm{mean}}$ being an approximation of $U_{\theta,\mathrm{mean}}$. The total root mean square velocity is calculated as

$$V_{\mathrm{rms}} = \sqrt{\frac{1}{3}[U^2_{x,\mathrm{rms}} + U^2_{r,\mathrm{rms}} + U^2_{\theta,\mathrm{rms}}]} \quad (3)$$

$$\approx \sqrt{\frac{1}{3}[U^2_{x,\mathrm{rms}} + U^2_{r,\mathrm{rms}} + (\frac{U_{x,\mathrm{rms}} + U_{r,\mathrm{rms}}}{2})^2]} \quad (4)$$

We note that the equivalence ratios are only slightly different here compared to equivalence ratios of the mean flame images shown in Fig. 7 and these still correspond to the same configurations.

The flow field at all equivalence ratios exhibits negative axial velocity regions, namely the recirculation zones (IRZ and ORZ). These regions are bounded by the ISL and OSL. However, the flow strength, the presence and location of stagnation points, as well as the relative size of recirculation zones are among the major differences between different flame macrostructures.

Nonreacting Flow. The cold flow field shows the existence of a stagnation point around the sudden expansion plane close to the centerline. The IRZ extends downstream away from the field of view with a weak negative axial velocity. This field of view does not allow to conclude on whether this recirculation zone closes downstream or not. Two counter rotating vortices are observed on the shear layer one inlet diameter downstream of the stagnation point, contributing in average to the flow in and out of the recirculation zone. These two vortices in the plane are likely to be part of the same toroidal vortex ring. Moreover, a flow–flow impingement point is observed just downstream of the upper vortex along the inner shear layer. This point appears like an off-centered downstream stagnation point, further highlighting the cylindrical asymmetry of the flow at these conditions. This flow is similar to swirling flows with asymmetric helical mode of vortex breakdown reported in the literature for swirling flows [14,22]. In fact, this flow exhibit a strong PVC oscillating at a frequency around $f_{\mathrm{PVC}} = 105$ Hz or a Strouhal number $\mathrm{St}_{\mathrm{PVC}} = f_{\mathrm{PVC}} D_{\mathrm{in}}/U_{\mathrm{in}} \approx 0.5$.

Flame I. The mean flow field in flame I ($\phi = 0.51$) is similar to the cold flow. In the range of equivalence ratio where macrostructure I exists, which is very close to the LBO limit ($\phi_{\mathrm{LBO}} \approx 0.47$), the rate of heat release is relatively low and the effect of combustion on the flow dynamics is relatively weak. The major difference is the strength of the back flow as well the incoming jet reattachment length. The PVC is still observed for this flame with a slight shift upward in frequency.

Flame III. When flame III is established, the flow field is dramatically different from the nonreacting and flame I flow fields. A clearly defined IRZ bubble appears. While the upstream stagnation points disappear from the field of view, the downstream one's position becomes close to the combustor's centerline. An additional vortical structure appears in the middle of the IRZ, in addition to the two vortices on the inner shear layer. The vortical structures of the IRZ lead to a two-lobe structure as shown by the axial zero velocity contour. These flame and flow field are characterized by their symmetry when compared to previous cases (cold flow and flame I).

Flame IV. The streamlines for $\phi = 0.65$ show the mean velocity after the transition of the flame to the ORZ. A comparison with the flow field at $\phi = 0.6$ shows a more compact IRZ without the two-lobe structure mentioned above. In addition, a larger incoming annular jet is observed along with the reappearance of the upstream stagnation point.

Increasing heat release level through the increase in equivalence ratio changes the flame macroscale structure along with the flow field. The swirling flow field seems to shift from a spiral asymmetric mode dominated by a PVC with a clearly defined frequency—the PVC being observed in cold flow and flame I—to an axisymmetric vortex breakdown with a bubble-shaped IRZ, observed for higher equivalence ratio flames. The types of vortex breakdown observed in our experiments and their characteristics extracted from PIV fit fairly well the description of the different types of vortex breakdown reported by Lucca-Negro and O'Doherty [14]. The suppression of the PVC has also been previously

Table 2 Combustion dynamics and mean flame configurations in the long versus short combustor

Long combustor				Short combustor			
Equivalence ratio	Dominant frequency	Dynamic mode	Mean flame configuration	Mean flame configuration	Dynamic mode	Dominant frequency	Equivalence ratio
0.50–0.54	Broadband	Stable	I	I	Stable	Broadband	0.50–0.535
0.54–0.555	Broadband	Stable	II	II	Stable	Broadband	0.535–0.545
0.555–0.61	38–40 Hz	Quasi-stable	III	III	Stable	Broadband	0.545–0.61
0.61–0.64	40–42 Hz	First unstable mode	IV	ORZ flickering	Stable	Broadband	0.61–0.64/0.65
0.64/0.65–0.67	48–55 Hz	Quasi-stable	IV	IV	Stable	Broadband	0.64–0.71
0.67–0.75	117–129 Hz	Second unstable mode	V	V	Unstable	120–132 Hz	0.71–0.75

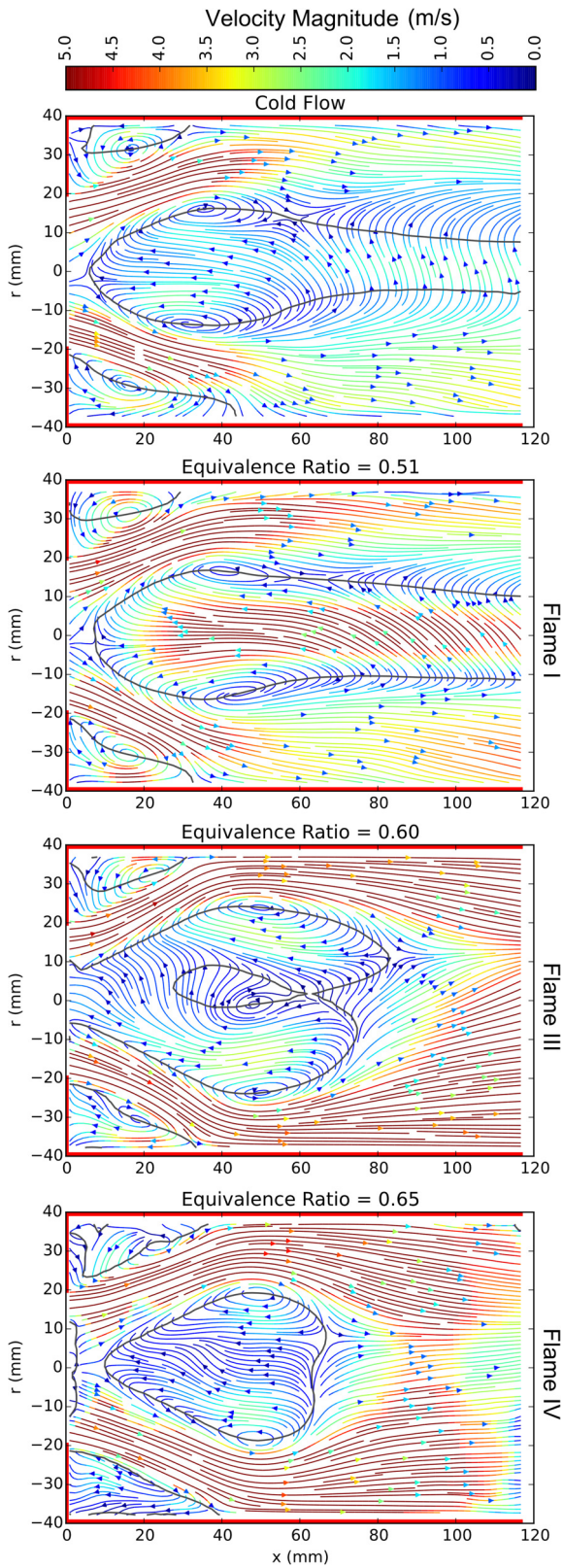

Fig. 10 Mean velocity streamlines colored by velocity magnitude for nonreacting flow and flame macrostructures I ($\phi = 0.51$), III ($\phi = 0.60$), and IV ($\phi = 0.65$)

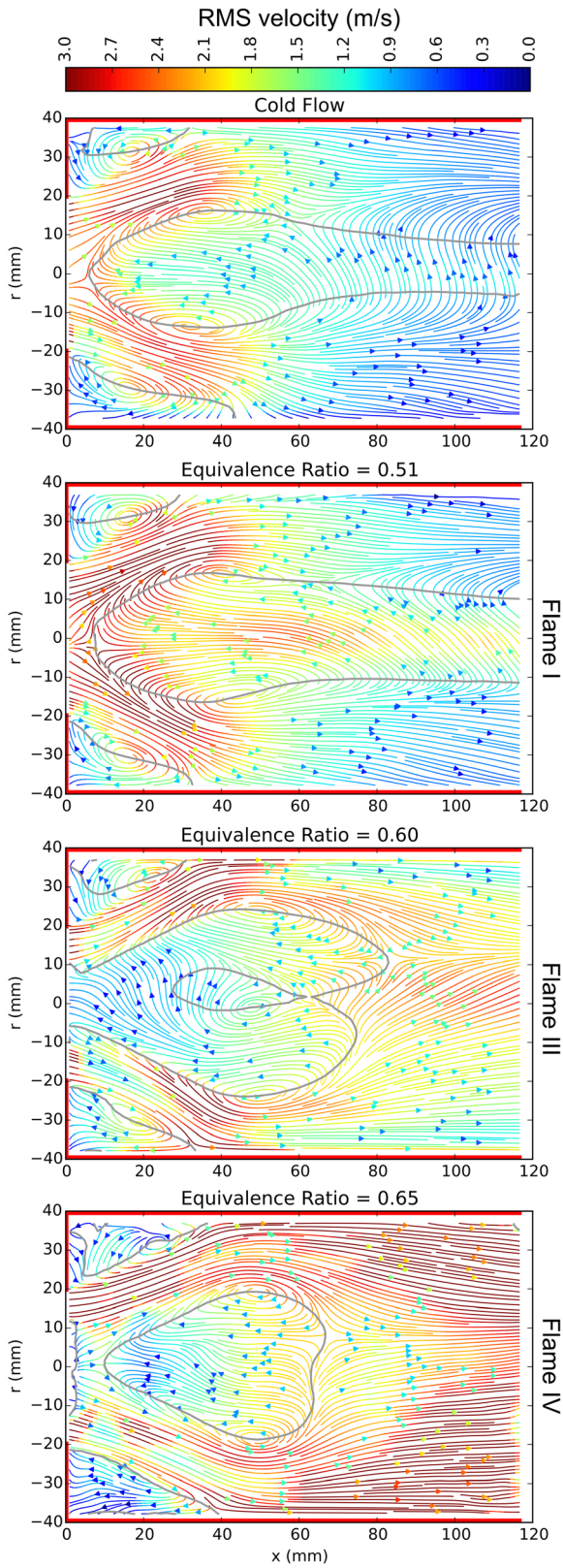

Fig. 11 Mean velocity streamlines colored by total rms velocity for nonreacting flow and flame macrostructures I ($\phi = 0.51$), III ($\phi = 0.60$), and IV ($\phi = 0.65$)

observed but there is still a lack of consensus around the mechanisms underlying it. As the equivalence ratio is raised, the heat release increases and induces a higher incoming jet velocity. Heat release only affects the meridional (axial–radial) velocity but not the swirling component. Thus, one expects the swirl strength to decrease. This could not be confirmed here as the azimuthal component of velocity was not measured. This decrease in swirl strength could potentially be the reason behind the shift from a strong asymmetric helical mode to the symmetric bubble mode of

vortex breakdown instability, but this requires further investigation which is outside the scope of the current study.

Finally, the angle between the centerline and the mean incoming jet angle and its dependency on the equivalence ratio is plotted in Fig. 12. The incoming jet angle and its reattachment length's corollary change as a function of equivalence ratio. The net effect of ORZ expansion and increased compactness of the IRZ lead to a larger width incoming jet. The jet forms a narrower angle in the mean flow sense for the cold flow and, as the equivalence ratio increases, the angle increases. This effect has been previously numerically studied [23]. This trend is reversed for flame IV. This can be explained by the appearance of expanded hot products in the ORZ forcing the incoming jet inward towards the combustor's centerline.

3.3 Transition to ORZ Flame (III to IV). The previous analysis established a relationship between the different dynamic modes and the mean flame macrostructures observed. We saw that even when decoupling the reacting flow from the acoustic field, the flame brush spatial distribution still changes and transitions occur around the same equivalence ratio. The onset of instability at the fundamental frequency of the long combustor is of particular interest as it is associated with a specific event: the change in flame configuration from flame III to IV through an intermittent appearance of the flame in the ORZ (see Fig. 8) as highlighted earlier. In this section, we aim to explore this transition in more detail.

Using the shortened version of the combustor—for which instability was suppressed—we increase the equivalence ratio following again the same procedure. When reaching the flickering interval (shown in Fig. 9) the equivalence ratio is maintained and IR-filtered high speed images are recorded at a frame rate of 200 frames per second, an exposure time of 5 milliseconds, from $\phi = 0.59$ to $\phi = 0.66$, i.e., a range encompassing the transition between flame III and flame IV. Flame chemiluminescence intensity is extracted from a selected region in the ORZ, shown in Fig. 13, and spatially averaged over that region. The probability of a flame to be present in the ORZ is plotted in this range of equivalence ratio (see Fig. 14). This probability is defined as the number of snapshot where a nonzero ORZ intensity is recorded divided by the total number of frames. As the equivalence ratio is raised the probability of having a flame in the ORZ increases, with an inflection point at $\phi = 0.63$. Passed $\phi = 0.64$, the flame becomes continuously present in the ORZ as reflected by its probability $P_{\phi=0.65} = 0.97$.

The ORZ space-averaged flame intensity is plotted over time in Fig. 15 for $\phi = 0.60, \phi = 0.63, \phi = 0.66$ along with its discrete

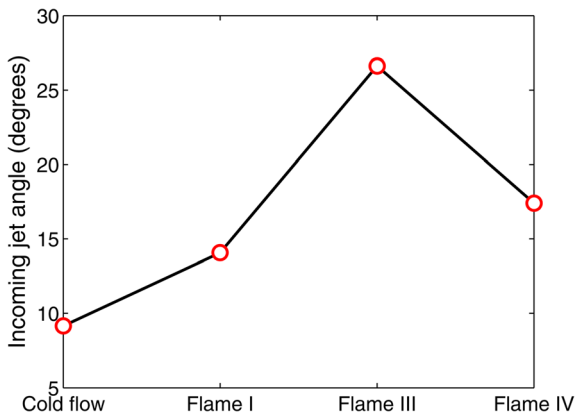

Fig. 12 Comparison of incoming jet angle, defined using the combined axial–radial maximum velocity magnitude, for non-reacting flow and flame macrostructures I ($\phi = 0.51$), III ($\phi = 0.60$), and IV ($\phi = 0.65$)

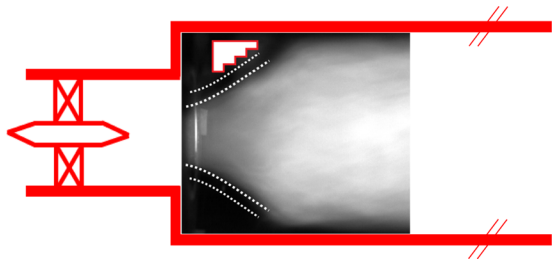

Fig. 13 Flame image at $\phi = 0.62$, recorded with an exposure time of 5 ms, showing a schematic of the ORZ analysis box and the shear layers around the incoming swirling jet

Fourier transform using the fast Fourier transform (FFT) algorithm. The spectral analysis shows the presence of low frequency events in the range ~(1 Hz–10 Hz) and a clear tone occurring around 28 Hz. The Strouhal number associated with this peak at 28 Hz, based on the inlet diameter and the inlet bulk velocity, is St ≈ 0.12. From the temporal variation of the signal, we see that the low frequency events correspond to the re-appearance of the flame in the ORZ. In some of these appearance instances, the flame reaching the ORZ is quickly extinguished. In other instances, the flame is advected along the outer recirculation vortex ring, survives and rotates around the combustor's centerline as it propagates. This rotation motion was highlighted in our previous work and associated with the 28 Hz frequency peak. It was also found to be dominated by hydrodynamics and not fuel dependent [24]. The two frequency bands observed here using flame chemiluminescence data were also confirmed based on the velocity field: we performed a dynamic mode decomposition (DMD) of the instantaneous PIV measurements [25] to extract dominant dynamics of the reacting flow for the different flame macrostructures. This approach showed that the transition from configuration III to IV is associated with these frequency bands, as well. In addition, the low frequency band was also linked to changes in the IRZ structure [25]. Low frequency motion of the IRZ has been previously highlighted in the bubble-type vortex breakdown [14]. Most probably, this low frequency motion is related to the cyclic filling and emptying of the vortex breakdown bubble volume that has been previously reported by Brucker and Althaus [26] as well as Billant et al. [27]. During this motion, the incoming fluid through the annular jet around the bubble is entrained inside the bubble from the downstream part of the bubble then ejected from it from the upstream part. Billant et al. [27] proposed an approximation for the frequency of this filling and emptying cycle based on a simple scaling analysis: $f \propto V/\dot{Q}$ with V being the volume of the inner recirculation bubble and $\dot{Q}$ being the volumetric flow rate into the bubble. In the case of the swirling flow setup studied in this paper,

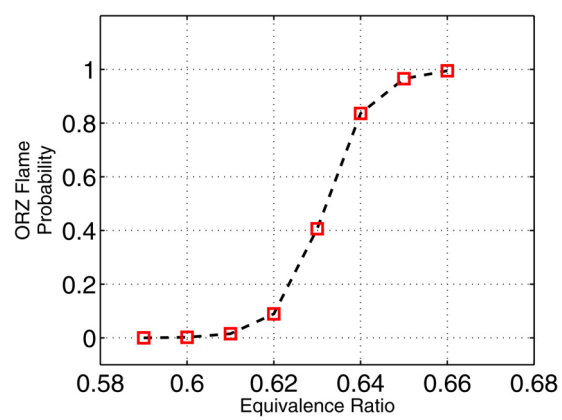

Fig. 14 ORZ flame intensity probability during transition from flame III to IV

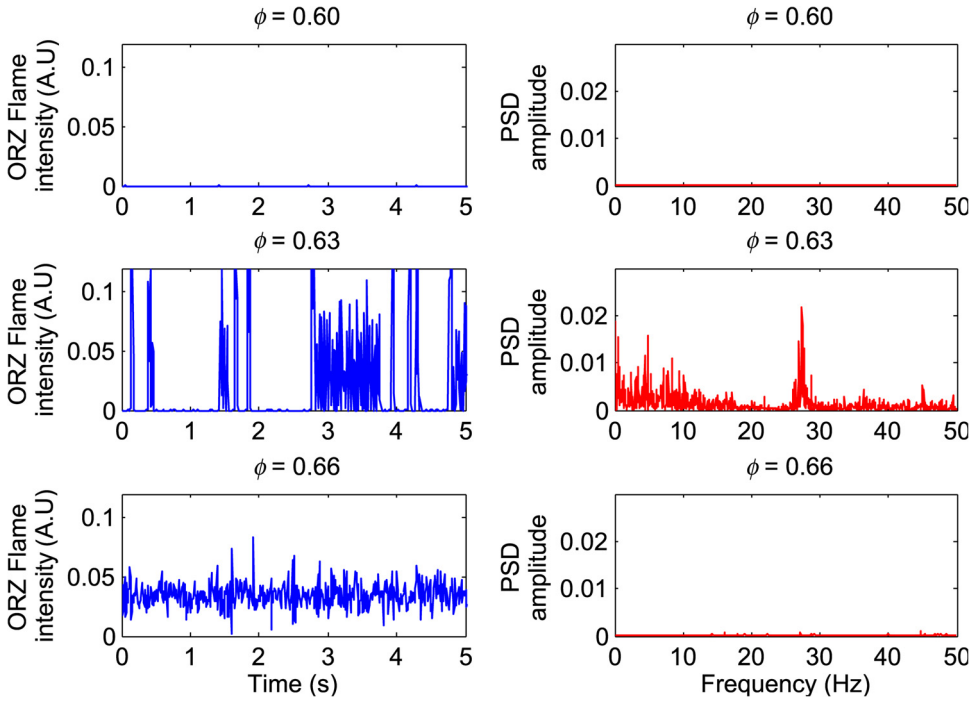

Fig. 15 ORZ flame spectral analysis for $\phi = 0.60$ (flame III), $\phi = 0.63$ (flame III $\leftrightarrow$ IV), and $\phi = 0.66$ (flame IV): space-averaged IR filtered chemiluminescence intensity signal in ORZ (left) and its fast Fourier transform (right)

with a Reynolds number of 20,000, this frequency could be approximated as follows:

$$f \approx \frac{\dot{Q}_{\text{bubble}}}{V_{\text{bubble}}} \tag{5}$$

$$\approx \frac{\alpha \dot{Q}_{\text{total}}}{V_{\text{bubble}}} \tag{6}$$

$$\approx \frac{\alpha(\pi D_{\text{in}}^2) U_{\text{bulk,in}}}{\frac{4}{3}\pi D_{\text{in}}^3} \tag{7}$$

$$\approx 40\alpha \tag{8}$$

With α the fraction of the volumetric flow rate that is recirculated through the IRZ and approximating the vortex breakdown bubble as a sphere with radius D_{in}. Assuming α in the range of 0.1–0.4, i.e., between 10% and 40% of the inlet volumetric flow rate recirculates through the inner bubble then the low frequency pulsation motion of the IRZ is in the range of 4–16 Hz which is of the order of the frequency measured by chemiluminescence as well as the frequency extracted from the DMD analysis.

4 Concluding Remarks

In this paper, we explored the relationship between the combustion dynamic modes and mean flame configurations or macrostructures as a function of the equivalence ratio. We used a confined premixed swirl-stabilized dump combustor similar to those found in modern gas turbines. The fuel (methane), the swirl number ($S = 0.7$), the Reynolds number ($\text{Re}_{D_{\text{in}}} = 20,000$), the inlet temperature (300 K) and pressure (atmospheric) were held constant. By breaking the feedback loop between the heat release rate and the acoustic pressure fluctuations, through the modification of the resonant frequencies of the combustor without altering the underlying flow, the mean flame configurations and the transitions between them could be analyzed. We reached the following conclusions:

(1) Dynamic modes in the long combustor are mostly associated with specific mean flame brush spatial distributions. Transitions in the flame macroscale structures are in most instances accompanied by changes in dynamic modes. In particular, the first appearance of a continuous flame front in the ORZ coincides with the onset instability at the long combustor's fundamental frequency.
(2) The observed sequence of flame macrostructures is not only the same in both the initial (long) and the modified (short) combustor, but the transitions (for configurations I, II, III, and IV) occur at similar equivalence ratios.
(3) High speed, relatively low exposure time chemiluminescence analysis of the transition between configuration III and IV in the short combustor (where this transition occurs in a thermo-acoustically stable way) shows that this transition is gradual (over $\Delta\phi \sim 0.03$) and is characterized by an intermittent appearance of the flame in the ORZ. The probability of an existing flame front in the ORZ increases as the equivalence ratio is raised. This ORZ flame flickering phenomenon was shown to be associated with two distinct frequency bands: a low frequency broadband mainly in the range $\sim$(1 Hz–10 Hz), likely due to the IRZ motion, and a narrow band centered around 28 Hz (St $\approx$ 0.12).

In the future, we plan to investigate further the intermittent flame transition to the ORZ, in particular the transition mechanism. The mechanisms underlying the other flame macrostructure transitions will be investigated as well. Planar laser-induced fluorescence imaging of OH radicals (OH-PLIF) measurements as well as numerical tools (large eddy simulations) will be used to reach this goal.

Acknowledgment

This work was supported by the King Fahd University of Petroleum and Minerals (KFUPM) and King Abdullah University of Science and Technology (KAUST) in Saudi Arabia, under the Grant Nos. R12-CE-10 and KUS-110-010-01, respectively.

Nomenclature

FFT = fast Fourier transform algorithm
IRZ = inner or inside recirculation zone
ISL = inner or inside shear layer
NO_x = nitrogen oxides
ORZ = outer or outside recirculation zone
OSL = outer or outside shear layer
α_{quartz} = thermal diffusivity of quartz in m s^{-2}
ϕ = equivalence ratio

References

[1] Durox, D., Moeck, J. P., Bourgouin, J.-F., Morenton, P., Viallon, M., Schuller, T., and Candel, S., 2013, "Flame Dynamics of a Variable Swirl Number System and Instability Control," Combust. Flame, **160**(9), pp. 1729–1742.

[2] Richards, G., McMillian, M., Gemmen, R., Rogers, W., and Cully, S., 2001, "Issues for Low-Emission, Fuel-Flexible Power Systems," Progress Energy Combust. Sci., **27**(2), pp. 141–169.

[3] Janus, M., Richards, G., Yip, M., and Robey, E., 1997, "Effects of Ambient Conditions and Fuel Composition on Combustion Stability," U.S. Department of Energy, Federal Energy Technology Center, Morgantown, WV, Technical Report No. DOE/FETC/C-97/7283.

[4] Lieuwen, T., McDonell, V., Petersen, E., and Santavicca, D., 2008, "Fuel Flexibility Influences on Premixed Combustor Blowout, Flashback, Autoignition, and Stability," ASME J. Eng. Gas Turbines Power, **130**(1), p. 011206.

[5] Lieuwen, T. C., Yetter, R., and Yang, V., 2009, *Synthesis Gas Combustion Fundamentals and Applications*, CRC Press, Boca Raton, FL.

[6] Ferguson, D., Straub, D., Richards, G., and Robey, E., 2007, "Impact of Fuel Variability on Dynamic Instabilities in Gas Turbine Combustion," Fifth U.S. Combustion Meeting, San Diego, CA, Mar. 25–28.

[7] Kim, K. T., Lee, J. G., Lee, H. J., Quay, B. D., and Santavicca, D. A., 2010, "Characterization of Forced Flame Response of Swirl-Stabilized Turbulent Lean-Premixed Flames in a Gas Turbine Combustor," ASME J. Eng. Gas Turbines Power, **132**(4), p. 041502.

[8] Fritsche, D., Füri, M., and Boulouchos, K., 2007, "An Experimental Investigation of Thermoacoustic Instabilities in a Premixed Swirl-Stabilized Flame," Combust. Flame, **151**(1), pp. 29–36.

[9] Candel, S., 2002, "Combustion Dynamics and Control: Progress and Challenges," Proc. Combust. Inst., **29**(1), pp. 1–28.

[10] Huang, Y., and Yang, V., 2009, "Dynamics and Stability of Lean-Premixed Swirl-Stabilized Combustion," Progress Energy Combust. Sci., **35**(4), pp. 293–364.

[11] Schefer, R., Wicksall, D., and Agrawal, A., 2002, "Combustion of Hydrogen-Enriched Methane in a Lean Premixed Swirl-Stabilized Burner," Proc. Combust. Inst., **29**(1), pp. 843–851.

[12] Chterev, I., Foti, D., Seitzman, J., Menon, S., and Lieuwen, T., 2012, "Flow Field Characterization in a Premixed, Swirling Annular Flow," AIAA Paper No. 2012-0450.

[13] Chterev, I., Foley, C., Noble, D., Ochs, B., Seitzman, J., and Lieuwen, T., 2012, "Shear Layer Flame Stabilization Sensitivities in a Swirling Flow," ASME Paper No. GT2012-68513.

[14] Lucca-Negro, O., and O'Doherty, T., 2001, "Vortex Breakdown: A Review," Progress Energy Combust. Sci., **27**(4), pp. 431–481.

[15] Speth, R. L., and Ghoniem, A. F., 2009, "Using a Strained Flame Model to Collapse Dynamic Mode Data in a Swirl-Stabilized Syngas Combustor," Proc. Combust. Inst., **32**(2), pp. 2993–3000.

[16] LaBry, Z. A., Shanbhogue, S. J., Speth, R. L., and Ghoniem, A. F., 2011, "Flow Structures in a Lean-Premixed Swirl-Stabilized Combustor With Microjet Air Injection," Proc. Combust. Inst., **33**(1), pp. 1575–1581.

[17] LaBry, Z. A., Shanbhogue, S. J., Speth, R. L., and Ghoniem, A. F., 2010, "Instability Suppression in a Swirl-Stabilized Combustor Using Microjet Air Injection," AIAA Paper No. 2010-1524.

[18] Shroll, A. P., Shanbhogue, S. J., and Ghoniem, A. F., 2012, "Dynamics and Stability Limits of Syngas Combustion in a Swirl-Stabilized Combustor," ASME J. Eng. Gas Turbines Power, **134**(5), p. 051504.

[19] Villarreal, R., and Varghese, P. L., 2005, "Frequency-Resolved Absorption Tomography With Tunable Diode Lasers," Appl. Opt., **44**(31), pp. 6786–6795.

[20] Speth, R. L., Altay, H. M., Hudgins, D. E., and Ghoniem, A. F., 2008, "Dynamics and Stability Limits of Syngas Combustion in a Swirl-Stabilized Combustor," ASME Paper No. GT2008-51023.

[21] Moeck, J. P., Bourgouin, J.-F., Durox, D., Schuller, T., and Candel, S., 2012, "Nonlinear Interaction Between a Precessing Vortex Core and Acoustic Oscillations in a Turbulent Swirling Flame," Combust. Flame, **159**(8), pp. 2650–2668.

[22] Syred, N., 2006, "A Review of Oscillation Mechanisms and the Role of the Precessing Vortex Core (PVC) in Swirl Combustion Systems," Progress Energy Combust. Sci., **32**(2), pp. 93–161.

[23] Underwood, D. S., Waitz, I. A., and Greitzer, E. M., 2000, "Confined Swirling Flows With Heat Release and Mixing," J. Propul. Power, **16**(2), pp. 169–177.

[24] Taamallah, S., LaBry, Z. A., Shanbhogue, S. J., and Ghoniem, A. F., 2014, "Thermo-Acoustic Instabilities in Lean Premixed Swirl-Stabilized Combustion and Their Link to Acoustically Coupled and Decoupled Flame Macrostructures," Proc. Combust. Inst. (in press).

[25] LaBry, Z. A., Taamallah, S., Kewlani, G., Shanbhogue, S. J., and Ghoniem, A. F., 2014, "Mode Transition and Intermittency in an Acoustically Uncoupled Lean Premixed Swirl-Stabilized Combustor," ASME Paper No. GT2014-27266.

[26] Brucker, C., and Althaus, W., 1995, "Study of Vortex Breakdown by Particle Tracking Velocimetry (PTV) Part 3: Time-Dependent Structure and Development of Breakdown-Modes," Exp. Fluids, **18**(3), pp. 174–186.

[27] Billant, P., Chomaz, J., and Huerre, P., 1998, "Experimental Study of Vortex Breakdown in Swirling Jets," J. Fluid Mech., **376**, pp. 183–219.